Remarkably high performance of clew-like ZnO superstructure in reactive adsorption desulfurization

Peng Bai[1*], Bowen Liu[1], Pingping Wu[1], Rooh Ullah[1], Wei Xing[2] and Zifeng Yan[1*]

ABSTRACT In this study, a clew-like ZnO superstructure was synthesized by a copolymer-controlled self-assembly homogeneous precipitation method. Ni was impregnated to the clew-like ZnO superstructure to obtain Ni/ZnO adsorbents. The synthesized materials were characterized by scanning electron microscopy, transmission electron microscopy, N_2 sorption, X-ray diffraction, Fourier transform infrared spectrometry, and H_2-temperature programmed reduction techniques. The reactive adsorption desulfurization (RADS) performance of the adsorbents was evaluated in a fixed bed reactor using thiophene in *n*-octane as a model fuel. Sample Ni/ZnO-4h exhibits a remarkably high performance with a sulfur capacity of 189.1 mg S g^{-1}, which is above 6 times that of the one prepared with commercial ZnO. Characterization results show that the morphology changes from micro-clews to large solid sticks with the increase of the crystallization time. The loose and open architecture of the clew-like ZnO superstructure facilitates the diffusion of reactants/products, and prevents the adsorbent particles from breakage by supplying space for the volume expansion during the RADS process. The small nanoparticles in ZnO nanostrips result in a high sulfur adsorption capacity and also favor the dispersion of Ni, leading to an excellent RADS performance.

Keywords: ZnO, reactive adsorption desulfurization, nanostructure, adsorbent

INTRODUCTION

Fossil fuels contain significant quantity of organic sulfur compounds, which are the major source of detrimental SO_x and particulate pollutions [1]. The desulfurization of fossil fuels gains an increasing attention for more stringent environmental regulations and legislation on the production of clean fuels [2–4]. According to the Euro V emission standard, the sulfur content of transportation fuels is regulated to be less than 10 ppm [5]. However, it is difficult for the traditional industrial hydrodesulfurization (HDS) process to reduce the sulfur content to such low level especially for the thiophenes and aromatic thiophenes rich fuels, due to the steric hindrance effect [6]. Furthermore, H_2S engendered during the HDS process is easy to react with olefins in gasoline to produce thiols, creating difficulties in the ultra-deep desulfurization of gasoline. Therefore, to reduce the sulfur content in gasoline below 10 ppm, it is necessary to increase the severity of HDS process, which results in the excessive saturation of olefins, causing the loss in octane value of gasoline. Alternative technologies, such as adsorption desulfurization [7–9], oxidation desulfurization [10,11], extraction [12,13] and bio-catalytic treatment [14,15] have been developed. Among them, the reactive adsorption desulfurization (RADS) using a solid adsorbent is considered to be the most effective approach for the ultra-deep desulfurization of gasoline [16].

The origin of RADS technology could be traced back to 1920s, when some metal oxides such as ZnO, CaO and MnO_2 were found to show good adsorption performance for H_2S and later applied in the desulfurization of liquid fuel [17,18]. Tawara *et al.* [19] utilized the metal oxide supported Ni adsorbent for the RADS process, including Ni/Al_2O_3 and Ni/ZnO. It was found that Ni/Al_2O_3 catalyst exhibited a better activity than that of catalyst Ni/ZnO, while Ni/ZnO exhibited a higher sulfur capacity due to the storage of H_2S by ZnO, which opened ways for the design of adsorbents with high sulfur capacities. Following this pioneer work, a significant amount of efforts have been made for the development of Ni/ZnO based adsorbents [20–22]. By studying the desulfurization mechanism of thiophenic compounds [9,22,23], the RADS process using Ni/ZnO adsorbent was found to combine

[1] State Key Laboratory of Heavy Oil Processing, PetroChina Key Laboratory of Catalysis, College of Chemical Engineering, China University of Petroleum (East China), Qingdao 266580, China
[2] College of Science, China University of Petroleum (East China), Qingdao 266580, China
* Corresponding authors (emails: baipeng@upc.edu.cn (Bai P); zfyancat@upc.edu.cn (Yan Z))

advantages of both HDS and adsorption desulfurization [24–26]. As revealed, organic sulfur compounds in the feed firstly decompose on the surface of Ni particles to form Ni_3S_2 [27]. In the presence of H_2, Ni_3S_2 is converted to H_2S and Ni sites are restored to Ni^0. ZnO, as the sulfur acceptor, reacts with H_2S and is transformed to ZnS. After regeneration in O_2 atmosphere, ZnO is regenerated to complete a continuous RADS-regeneration cycle [28]. Bezverkhyy and co-workers [29–31] carried out a series of kinetics experiments on the RADS reactions with Ni/ZnO based adsorbents. It is found that the rate-limiting step is the decomposition of the organosulfur compounds on Ni species at the beginning. With the partial sulfidation of ZnO, the sulfur diffusion in ZnO becomes the rate-determining step. Based on the RADS mechanism, it is obvious that the dispersion of Ni species and ZnO morphology influence the RADS performance of adsorbents. Therefore, a ZnO structure that can improve the sulfur compound diffusion into ZnO particles and favor the nickel dispersion is desired [32]. As reported, smaller ZnO particles are favorable for the sulfur transfer from Ni to ZnO with lower activation energy, resulting in a higher ZnO conversion and a larger sulfur capacity. Besides, the smaller ZnO particle size would favor the Ni particle dispersion and enhance the interaction between Ni and ZnO, resulting in the formation of Ni-Zn alloy, which prohibits Ni particles from agglomeration [5]. Different nanostructured ZnO materials have been synthesized [33,34]. ZnO nanowires prepared by Gupta et al. [35] were tested in the RADS reaction. The adsorbent exhibits a high RADS activity and a large sulfur capacity, which is attributed to the easy sulfidation of ZnO nanowires and the fast sulfur transfer from Ni_xSZn_y to ZnO nanowires. Besides the particle size, the morphology of ZnO also has a significant effect on the RADS performance of the adsorbent. Liu et al. [36] synthesized a hierarchically structured poly-crystalline ZnO. Compared with that derived from the rod-shape ZnO particles, the adsorbent with the hierarchically structured ZnO exhibits a higher sulfur capacity.

In our previous work [37], a clew-like ZnO superstructure was synthesized via a copolymer-controlled self-assembly approach (CCSA). The superstructure was constituted by ZnO nanostrips, which wrapped each other around a common axis in a clew-twisting way. The nanostrips with a thickness of ca. 50 nm are consisted of nanoparticles with sizes from 50 to 100 nm, and exhibit a porous structure with pore sizes in the range of 30–100 nm. The intersecting and stacking nanostrips form a loose and open three dimensional (3D) archi-

tecture, which is favorable for the diffusion of reactants/ products in the clews and also helps to alleviate the aggregation of adjacent nanostrips during the RADS process. Therefore, this unique superstructure may exhibit a superior RADS performance. In this work, we synthesized the ZnO superstructures using the CCSA approach and varied the morphology of ZnO by changing the crystallization time. The Ni/ZnO adsorbents were prepared using an impregnation method. The RADS performance of adsorbents was evaluated in the reactive adsorption desulfurization of a model fuel and compared with that prepared with a commercial ZnO. By combining characterization results from a variety of techniques, the relationship between the structural properties of adsorbents and their RADS performance was revealed.

EXPERIMENTAL SECTION

Materials preparation
The ZnO superstructure was synthesized through a CCSA method according to our previous procedure [37]. In a typical synthesis, 2.32 g of $(PEO)_{20}(PPO)_{70}(PEO)_{20}$ (P123) was dissolved in 60 mL of deionized water, followed by the addition of 7.2 g of urea and 5.95 g of $Zn(NO_3)_2 \cdot 6H_2O$ with continuous stirring for 30 min. Then, the solution was transferred into a stainless steel autoclave with a Teflon liner and crystallized in an oven at 100°C for different times (4, 8, 17 and 48 h). White precipitates engendered were filtered, washed for several times with deionized water and dried in an oven for 12 h at 80°C. Finally, the white solids were calcined at 500°C for 2 h. The white and yellowish powders before and after calcination were denoted as ZCH-xh and ZnO-xh, respectively, where x represented the crystallization time.

The Ni/ZnO adsorbents (10 wt.% Ni) were prepared by an ultrasonic-aided incipient wetness impregnation method. In a typical procedure, 0.495 g of $Ni(NO_3)_3 \cdot 6H_2O$ was dissolved in 5 mL of tetrahydrofuran (THF), followed by adding 1 g of ZnO into the solution. The suspension was ultrasonically dispersed at 30°C for 1 h, then dried at 80°C overnight and calcined at 400°C for 1 h. The adsorbents obtained were denoted as Ni/ZnO-xh. For comparison, a Ni/ZnO adsorbent was prepared in the same way from a commercial ZnO (purchased from Sinopharm Chemical Reagent Co. Ltd) and denoted as Ni/ZnO-C.

RADS reactions
RADS experiments were carried out in a fixed bed reactor with a stainless steel column which had an internal di-

mension of 8 mm and a length of 250 mm. The model fuel with 3000 ppm sulfur was prepared using thiophene as a sulfur source and *n*-octane as the solvent. Before the reaction, the reactor was flushed by ethanol for 24 h to clean the thiophene remaining in the system. The flushing was conducted at 150°C with an ethanol flow rate of 0.5 mL min^{-1}. Then the whole system was purged with a N$_2$ gas flow (20 mL min^{-1}, 0.5 MPa) at 150°C for 24 h to clean up the whole system. After that, 1 g of fresh adsorbent (NiO/ZnO) was put in the center of the column and reduced by H$_2$ with a flow rate of 40 mL min^{-1} under 0.5 MPa at 400°C for 7 h. After the reduction, the temperature of reactor was reduced to 350°C and the pressure was increased to 1.0 MPa. The pre-heated model fuel was carried by H$_2$ and flowed through the adsorbents with a liquid hourly space velocity (LHSV) of 4 h^{-1}, and the H$_2$/Oil volume ratio was 400. The liquid product was cooled in a cryogenic ice trap, periodically collected and analyzed by a gas chromatograph (Bruker 450-GC) coupled with a pulsed flame photometric detector (PFPD). The sulfur capacity of the adsorbents at breakthrough points of 10 ppm (normalized by the adsorbent weight) was calculated based on [38]

$$S = \frac{v}{1000 m_{sorbent}} \int_0^t (C_0 - C_t) \mathrm{d}t, \tag{1}$$

where S is the mass of sulfur adsorbed per gram of adsorbent (mg S g^{-1}), C_0 is the initial sulfur concentration in the model fuel (mg L^{-1}), C_t is the sulfur concentration in the effluent at time t (min), v is the flow rate of model fuel (mL min^{-1}), and $m_{sorbent}$ is the weight of Ni/ZnO-xh adsorbent. The ZnO conversion of the adsorbent at the adsorption breakthrough point (10 ppm) was calculated by

$$X = 0.0029 S \times 100\%, \tag{2}$$

where X is the ZnO conversion to ZnS of the adsorbent at breakthrough point (10 ppm), and S is the sulfur capacity at the breakthrough point (10 ppm).

Characterization of materials

The N$_2$ adsorption was measured on a Micromeritics TRISTAR 3000 analyzer at 77 K. Before adsorption, samples were degassed at 300°C for 4 h under vacuum. The specific surface area of the samples was calculated by the Brunauer-Emmett-Teller (BET) method in the relative pressure range of 0.05–0.25. The pore size distribution (PSD) curves were derived from the desorption branches using the Barrett-Joyner-Halenda (BJH) method. The total pore volumes were calculated by the adsorption amount at P/P_0=0.993. X-ray powder diffraction

(XRD) patterns were obtained by a PANalytical X'Pert diffractometer with a Cu-Kα radiation generated at 35 kV and 40 mA. The scanning angle ranged from 20° to 70° with a scanning rate of 2° min^{-1}. Average crystallite sizes of the ZnO crystals were calculated from the XRD patterns using Debye-Scherrer equation

$$D = K\lambda / \beta \cos\theta, \tag{3}$$

where K is the Scherrer constant (K=0.89), λ is the X-ray wavelength, β is the peak width at the half maximum, and θ is the Bragg diffraction angle. The reducibility of samples was investigated by a hydrogen temperature programmed reduction (H$_2$-TPR) technique using a Chem-BET 3000 TPD/TPR analyzer (Autochem II, USA). The morphology of materials was investigated by a JEOL JSM-5600LV scanning electron microscope (SEM) and a JEOL JEM-2100UHR transmission electron microscope (TEM). Fourier transformed infrared (FT-IR) spectra of the adsorbents were measured on a Nicolet 6700 spectrometer coupled with a MCT liquid nitrogen cooling detector, and the samples were dehydrated at 300°C for 3 h and then subjected to pyridine adsorption for 24 h. After adsorption of pyridine, the samples were transferred into a vacuum oven at 150°C for 3 h to remove the physisorbed pyridine. Samples were then pressed into disks with a radius (R) of 1.0 cm. The amount of Lewis acid (L acid) was quantified according to the Equation (4) described elsewhere [39]

$$C(\text{pyridine on L acid sites}) = 1.42 IA(\text{L}) R^2 / W, \tag{4}$$

where C is the concentration of L acid sites (mmol g^{-1} catalyst), IA is the integrated absorbance of L acid band (cm^{-1}), R is the radius of catalyst disk (cm) and W is the weight of the disk (mg).

RESULTS AND DISCUSSION

### RADS performance of adsorbents

Figs 1, 2 show sulfur adsorption breakthrough curves and breakthrough sulfur capacities of adsorbents, respectively. As can be seen, the RADS activity of the adsorbents decreases with increasing the crystallization time of ZnO. Amongst all samples, sample Ni/ZnO-4h achieves the highest breakthrough time up to 25.5 h with a sulfur adsorption capacity up to 189.1 mg S g^{-1}. Compared with Ni/ZnO-4h, Ni/ZnO-8h, Ni/ZnO-17h and Ni/ZnO-48h achieve a shorter breakthrough time with a decreasing breakthrough sulfur adsorption capacity. Among all samples, the adsorbent prepared with the commercial ZnO presents the lowest RADS activity with a breakthrough time of 4.6 h and a sulfur adsorption capacity of
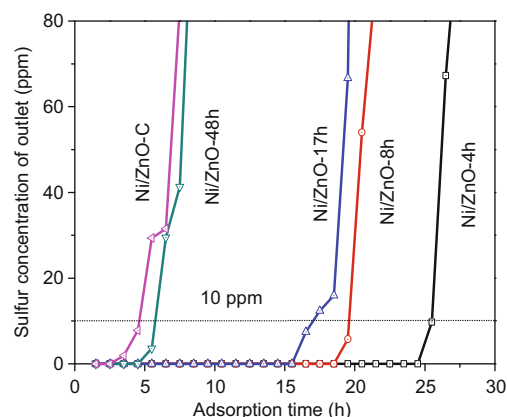
**Figure 1** Sulfur adsorption breakthrough (10 ppm) curves of adsorbents.

Table 1 ZnO conversion of different adsorbents to ZnS at the breakthrough point (10 ppm)

Adsorbents	ZnO conversion (%)
Ni/ZnO-4h	54.8
Ni/ZnO-8h	39.6
Ni/ZnO-17h	33.0
Ni/ZnO-48h	10.6
Ni/ZnO-C	8.3
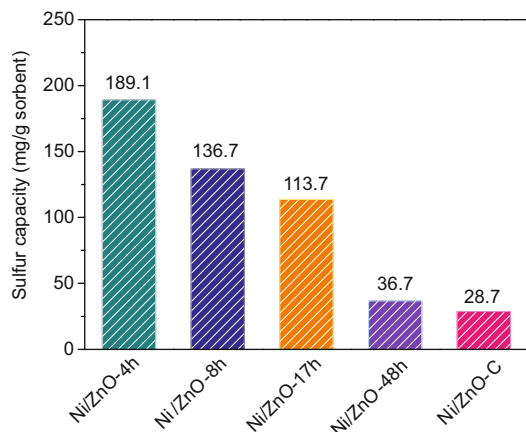
Figure 2 Breakthrough sulfur capacities of adsorbents.

28.7 mg S g^{-1}, which is only 15.2% of that of Ni/ZnO-4h. Calculated ZnO conversions of different adsorbents at breakthrough points are shown in Table 1. As is seen, among all adsorbents, sample Ni/ZnO-4h has the highest ZnO conversion of 54.8%. Furthermore, sample Ni/ZnO-4h also shows a higher capacity than most of other Ni/ZnO adsorbents with various types of ZnO reported before [35,36,40–42]. It was widely recognized that the RADS activity and sulfur adsorption capacity were closely
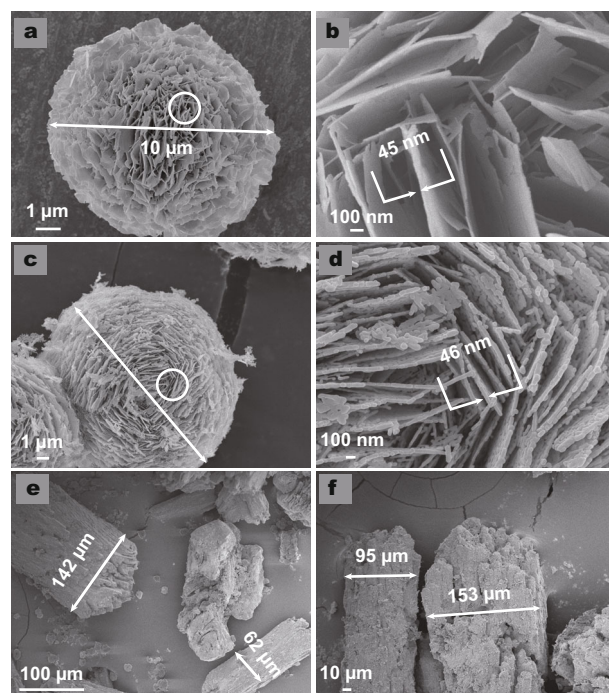
Figure 3 (a) SEM images of ZCH-4h; (b) magnified image of the circled area in image (a); (c) ZnO superstructure after calcining the ZCH precursor shown in (a); (d) magnified image of the circled area in (c); (e) ZCH-48h; (f) ZnO particles after calcining the ZCH precursor shown in (e).

related to the structure of Ni/ZnO adsorbents, including the dispersion of active sites (such as metallic Ni^0) for C–S bond cleavage [43], and particle size of ZnO for sulfur storage [5,22]. Compared with the commercial ZnO derived adsorbent, the superior RADS performance of Ni/ZnO-xh adsorbent may be related to the unique morphology and nanostructure of ZnO prepared using the CCSA approach.

SEM analysis

Our previous results have shown that the ZnO precursor before calcination is a monoclinic zinc carbonate hydroxide (ZCH) phase [Zn$_5$(CO$_3$)$_2$(OH)$_6$] (JCPDS card No. 00-19-1458) [37]. Fig. 3 shows the SEM images of ZCH precursors obtained at different crystallization times and corresponding ZnO materials after calcination. As can be seen, a clew-like 3D superstructure (Fig. 3a) was obtained after 4 h of crystallization with diameters ranging from 10 to 20 μm. This clew-like superstructure consists of nanostrips with a thickness of 30 to 50 nm, and the gaps between nanostrips are around 100 to 500 nm. After 48 h of crystallization, a solid rod-like morphology was obtained with a diameter of 78 to 180 μm. According to

morphology evolution experiments conducted before [37], it was believed that the clew-like superstructure of ZCH precursor was a metastable phase during the crystallization process. In order to reduce the surface energy of the superstructure, the shrinkage of segment gaps occurred due to the coagulation of the nanostrips and the surface-smoothing effect [44], resulting in the formation of the large rod-like structures.

After calcination, the ZnO-4h sample retains the same clew-like morphology as its ZCH precursor (Fig. 3c). The magnified SEM image (Fig. 3d) shows that the 3D clew-like ZnO superstructure consists of numerous thin ZnO strips with a thickness of about 50 nm, and the nanostrips are constituted by irregular ZnO nanoparticles connected with small bridges, exhibiting a nanoporous motif. Compared with the image shown in Fig. 3b, after calcination, the thickness of the strips remains almost the same, while a lot of pores appear in the strips due to the decomposition of ZCH. As the lattice parameters of ZnS are much higher than those of ZnO, which result in the volume expansion of adsorbents during the RADS process [45], the existence of the small bridges and pores in ZnO strips is favorable for protecting the adsorbents particles from breakage by supplying space for the volume expansion. Furthermore, the unique clew-like morphology alleviates the agglomeration of ZnO particles due to the gaps formed by the intersecting and stacking between different nanostrips, which allow the clew-like ZnO superstructure to remain loose and open, facilitating the diffusion of sulfur compounds into it. By contrast, the morphology of ZCH synthesized with a crystallization time of 48 h undergoes no obvious change after calcination. The obtained ZnO exhibits a similar rod-like dense structure as its ZCH precursor. Such dense structure brings about strong diffusion resistance to sulfur transfer into the inner part of the big rods, when the surface of the big rods is covered with ZnS during the RADS process [5,30]. Therefore, the superior RADS performance of the clew-like superstructure could be partially attributed to the loose structure and small ZnO nanoparticles endowed by this unique morphology.

XRD characterization

XRD patterns of the Ni/ZnO adsorbents before and after RADS are shown in Fig. 4. All fresh adsorbents contain two crystalline phases, a hexagonal wurtzite phase (ZnO, JCPDS card No. 01-74-0534) and a nickel oxide (JCPDS card No. 03-065-6920), which is in accordance with that reported by Babich [28]. For fresh adsorbents, with increasing the crystallization time, the intensity of ZnO
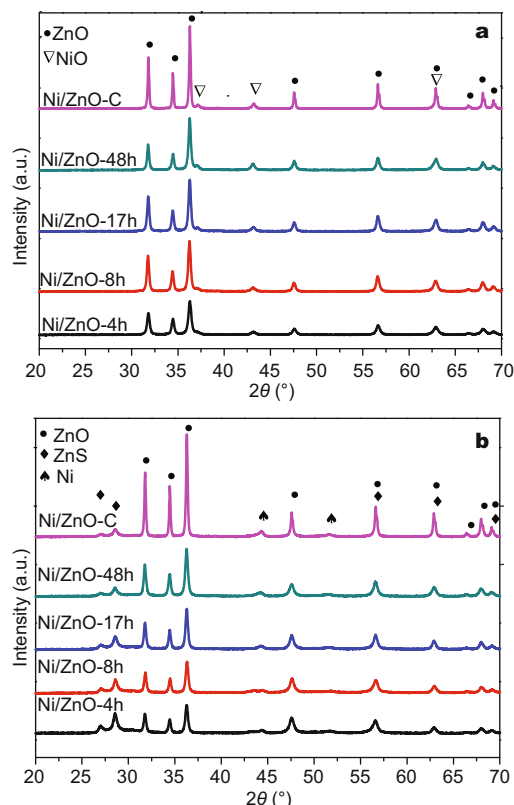

Figure 4 XRD patterns of the fresh (a) and spent (b) adsorbents.

peaks increases, and the crystallite size (shown in Table S1 (Supplementary information)) calculated by Debye-Scherrer equation [46], increases from 29 to 57 nm, which is attributed to the growth of ZCH crystals under hydrothermal synthesis conditions, consistent with the SEM results shown in Fig. 3.

The peak intensity of commercial ZnO is higher than those of synthesized samples, indicating the larger crystallite size of the commercial ZnO sample, which explains well the lowest RADS performance of Ni/ZnO-C among all samples. By contrast, an opposite trend is observed for NiO, i.e., the crystallite size of NiO decreases with the increase of the crystallization time (Table S1), which is partially attributed to the smaller ZnO particle size in ZnO superstructures. Besides, the loose and open superstructure of ZnO-4h could restrain the aggregation of NiO and ZnO particles [47] during the calcination process because of the gaps between different ZnO nanostrips. This result indicates that there are more metallic Ni^0 sites available for the C–S bond cleavage in adsorbents with ZnO synthesized at a shorter crystallization time, which accounts for the highest activity of sample

Ni/ZnO-4h among all prepared adsorbents.

As shown in Fig. 4b, after RADS, all samples exhibit a cubic ZnS phase (JCPDS card No. 03-065-1691). As is clearly seen, the intensity of ZnS peaks follows a decreasing trend with increasing the crystallization time and the calculated crystallite sizes of ZnS are shown in Table S1. The ZnO of 29 nm in sample Ni/ZnO-4h is transformed to ZnS of 57 nm, and the ZnO of 57 nm in sample Ni/ZnO-48h is converted to ZnS of 60 nm.

Therefore, the sample Ni/ZnO-4h has the biggest crystallite size change when converting from ZnO to ZnS among all adsorbents, which is in good agreement with the previous work [48] that the smaller ZnO particles have a higher conversion rate during RADS process compared with larger ones. Since the diffusion of sulfur in ZnO particles becomes the rate-limiting step when ZnO particles are partially sulfidized [31,49], the ZnO particles in Ni/ZnO-4h could be more easily sulfidized than those in other samples because of the smaller crystallite size, which agrees well with the calculated ZnO conversion results as shown in Table 1.

TEM analysis
TEM images of the fresh and spent adsorbents are shown in Fig. 5. As can be seen, Fig. 5a, b shows the microstructure of fresh sample Ni/ZnO-4h, and two kinds of lattice fringes with different spacings are identified, attributed to ZnO and NiO crystals. The porous structure of the nanostrips shown in Fig. 3 is observed, and the loose stacking of nanoparticles facilitates the diffusion of sulfur compounds in adsorbent particles, which partially explains the excellent activity of sample Ni/ZnO-4h in RADS. In comparison, as seen in Fig. 5c, d, the particle size of ZnO in sample Ni/ZnO-48h is much larger than that in sample Ni/ZnO-4h. The compact structure of sample Ni/ZnO-48h obstructs the diffusion of reactant/product molecules in the adsorbent and restrains the ZnO conversion to ZnS. TEM images of the spent sample Ni/ZnO-4h shown in Fig. 5e, f clearly demonstrate the presence of Ni, ZnS and ZnO crystals, consistent with the XRD results in Fig. 4b. The porous structure of ZnO nanostrips is retained after RADS and ZnO nanoparticles are not agglomerated or sintered to form bigger particles as that usually happens to ZnO nanoparticles, verifying the intrinsic advantages of the unique clew-like morphology. The voids between and within nanostrips could also protect the adsorbents particles from breakage caused by the volume expansion during ZnO sulfidation. It should be mentioned that Ni, ZnS and ZnO appear in a single particle, which partly supports the RADS me-
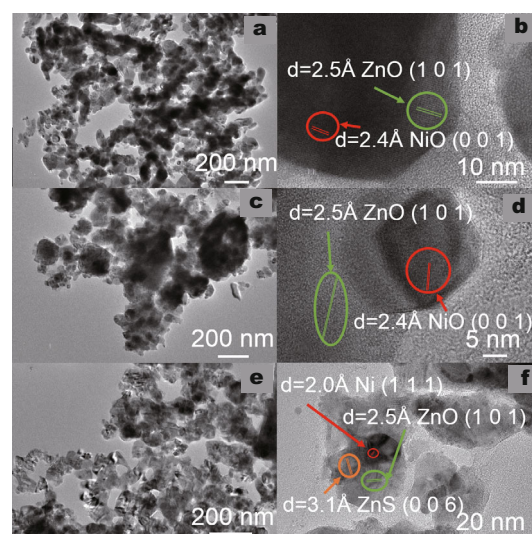
Figure 5 TEM images of the fresh Ni/ZnO-4h (a, b), fresh Ni/ZnO-48h (c, d), and spent Ni/ZnO-4h (e, f).

chanism proposed by Huang et al. [27]. During the RADS process, the thiophenic compound reacts with the active site Ni^0 on the ZnO and produced the Ni_3S_2. Subsequently, the sulfur in Ni_3S_2 is converted to H_2S in the hydrogen atmosphere, which is captured by ZnO and converted to ZnS. As a result, Ni is regenerated to Ni^0 and ready for the next RADS cycle.

Textual properties
Fig. S1 shows the N_2 adsorption-desorption isotherms and PSD curves of the fresh Ni/ZnO adsorbents. All adsorbents derived from the synthesized ZnO materials exhibit adsorption isotherms of between type-IV and type-III, indicating the adsorbents contain both mesopores and macropores. By contrast, sample Ni/ZnO-C shows a typical non-porous structure with a very low N_2 adsorption quantity, indicating the low surface area and low pore volume, which is confirmed by the results shown in Table S2. Except sample Ni/ZnO-C, all samples possess an H-3 hysteresis loop in the isotherms, evidencing that adsorbents are aggregates of plate-like particles giving rise to slit-shape pores [50], consistent with the nanostrip structure of ZnO as confirmed by SEM results. The PSD curves (Fig. S1b) show that all samples exhibit a bimodal pore size distribution. The sharp peak at around 3 nm is attributed to the tensile strength effect (TSE) and is not an indication of a real pore size distribution [51], while the larger and broad one in the range of 10–40 nm could be ascribed to the nanopores in the ZnO nanostrips [52].

In order to understand the variation in adsorbent's pore structure during the RADS process, the textural properties of the spent adsorbents were characterized and shown in Fig. S2. As can be seen, the N_2 adsorption amount decreased for all adsorbents after RADS, which may be attributed to the sulfur adsorption, sintering and/or coke deposition during the RADS process. As summarized in Table S2, there are obvious declines in both surface area and pore volume for all samples after RADS. With increasing the crystallization time, the variations in surface area and pore volume generally exhibit a decreasing trend, reflecting the difference in the reactivity of adsorbents. Since the lattice parameters of ZnS are larger than those of ZnO, the pore shrinkage and blockage will occur during the RADS process due to the ZnO volume expansion, resulting in the decrease in both surface area and pore volume. As sample Ni/ZnO-4h possesses the highest reactivity, it has the largest decrease in both surface area and pore volume after RADS. By contrast, sample Ni/ZnO-C exhibits the lowest variation in the pore structure due to its poor RADS activity.

FT-IR analysis
To study the structural variation of ZnO, FT-IR spectroscopy was applied to characterize the Ni/ZnO adsorbents before and after RADS (Fig. S3). As can be seen, FT-IR spectra of the fresh adsorbents (Fig. S3a) show a series of transmission bands at 664, 881 and 1385 cm^{-1}, which are assigned to Zn–O stretching vibrations [20,53,54]. After RADS, the characteristic peaks of ZnS (Fig. S3b) appear in all samples at around 623, 1049 and 1090 cm^{-1}. The band at 623 cm^{-1} is ascribed to the Zn–S stretching vibration [54,55], while that at 1049 cm^{-1} is assigned to the resonance interaction of S^{2-} on the ZnS crystals [20,54,56]. And the characteristic peak at around 1090 cm^{-1} is attributed to the stretching mode of ZnS [20,55]. Besides the characteristic Zn–O stretching bands, a peak at 1400 cm^{-1} assignable to the OH bending vibration in pure ZnO is observed for all spent samples, indicating the incomplete conversion of ZnO during the RADS process [53]. In a comparison, the intensity of the band at 1385 cm^{-1} clearly exhibits a decreasing trend with increasing the crystallization time, evidencing the higher ZnO conversion in adsorbents with ZnO synthesized at a shorter crystallization time, consistent with the results shown in Table 1.

As organosulfur compounds have strong tendency to adsorb on Lewis acid sites due to the basicity of lone electron pair, a high amount of Lewis acid sites are beneficial for the adsorption of thiophene molecules and
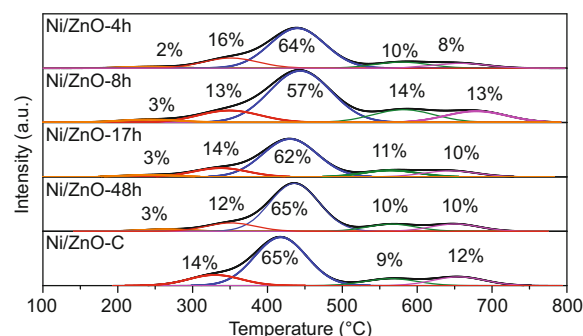

Figure 6 H$_2$-TPR profiles of the fresh adsorbents.

the subsequent C–S bond cleavage [57,58]. Therefore, the pyridine adsorption FT-IR analysis of adsorbents was conducted and shown in Fig. S4. As can be seen, all samples exhibit a band at 1450 cm^{-1} attributed to the 19bν (C–C) vibration of pyridine molecules adsorbed at the Lewis acid site [59,60]. Among all tested adsorbents (see Table S3), sample Ni/ZnO-4h possesses the highest concentration of Lewis acid (1.079 mmol g^{-1}) compared with other samples, which partially accounts for its high RADS activity.

H$_2$-TPR measurements
Since the breakage of C–S bonds is the rate-limiting step in the initial stage of RADS process and metal Ni^0 sites are responsible for the hydrogenolysis activity [31], the chemical state and reducibility of NiO strongly affect the reaction rate. Hence, we characterized the adsorbents by using H$_2$-TPR technique shown in Fig. 6.

As seen, all samples show three H$_2$ reduction peaks between 200 to 500°C in adsorbents with synthesized ZnO, whereas only two peaks appear for the adsorbent synthesized with the commercial ZnO. The appearance of these peaks is ascribed to the Ni^{2+}→Ni^0 reduction [27,61] of the nickel oxide which has different interactions with the ZnO [47]. The appearance of a weak peak at 250°C for all samples except sample Ni/ZnO-C is attributed to surface free Ni species. The broad peak at ca. 350°C and a large peak at ca. 450°C for all samples are attributed to the reduction of Ni^{2+} species weakly and strongly interacted with ZnO, respectively [62,63]. The percentage of the H$_2$ consumption peak at ca. 350°C was calculated for all samples, revealing that the ratio of the NiO reduced at ca. 350°C decreases with increasing the crystallization time and sample Ni/ZnO-4h has the highest amount (16%) of weakly interacted Ni^{2+} species among all the samples, which implies that the open morphology and small particle sizes of ZnO in sample ZnO-4h are favorable for the

dispersion of easily reducible Ni species. By contrast, the strongly interacted Ni^{2+} species with the reduction peak at ca. 450°C are not able to be reduced under mild pre-reduction conditions (400°C) [64], not contributing to the activity of adsorbents. The shoulder spanning from 500 to 750°C could be ascribed to the reduction of NiO species which are strongly attached to the ZnO crystals with the possible formation of Ni-Zn alloy [47]. Among all samples, Ni/ZnO-4h has the lowest ratio of H_2 consumption in this range, also indicating the easy reducibility of Ni species in this sample.

CONCLUSIONS

In this work, a clew-like ZnO superstructure was prepared and evaluated with the RADS of a model fuel with a high sulfur concentration. Among all test samples, sample Ni/ZnO-4h exhibits the best performance with a 189.1 mg S g^{-1} sulfur capacity, which is above 6 times that of the sample prepared with the commercial ZnO. By combining characterization results, the superior performance of Ni/ZnO-4h to others is clarified to be related to the following factors: (i) small ZnO particles decrease the diffusion resistance of sulfur diffusion in ZnO crystals and promote the dispersion of Ni; (ii) the loose and open architecture of the clew-like ZnO morphology enhances the diffusion of reactants/products in the adsorbent. Considering the facile synthesis route of the CCSA approach and the advantageous features of the clew-like superstructure, the ZnO prepared *via* the CCSA approach exhibits great potential in the design of industrial adsorbents with superior RADS performance.

1   Saiyasitpanich P, Lu M, Keener TC, *et al.* The effect of diesel fuel sulfur content on particulate matter emissions for a nonroad diesel generator. J Air Waste Manage Association, 2005, 55: 993–998

2   Shi Y, Zhang X, Wang L, *et al.* MOF-derived porous carbon for adsorptive desulfurization. AIChE J, 2014, 60: 2747–2751

3   Zhang Y, Yang Y, Lin F, *et al.* Improvement of adsorptive desulfurization performance of Ni/ZnO adsorbent by doping with Mn additive. Chin J Catal, 2013, 34: 140–145

4   Liu S, Zhang X, Zhang J, *et al.* MoS_2 with tunable surface structure directed by thiophene adsorption toward HDS and HER. Sci China Mater, 2016, 59: 1051–1061

5   Zhang Y, Yang Y, Han H, *et al.* Ultra-deep desulfurization via reactive adsorption on Ni/ZnO: the effect of ZnO particle size on the adsorption performance. Appl Catal B-Environ, 2012, 119-120: 13–19

6   Zhang XM, Shen BX, Hou XM, *et al.* Research on reactive adsorption desulfurization over metal oxides adsorbent. Energ Sources Part A-Recovery Utilization Environ Effects, 2015, 37: 209–216

7   Hou XM, Shen BX, Zhao JG. Reactive adsorption desulfurization of FCC gasoline over $NiO/ZnO-Al_2O_3-SiO_2$ in a fixed-fluidized bed reactor. Energ Sources Part A-Recovery Utilization Environ Effects, 2014, 36: 1517–1522

8   Srivastav A, Srivastava VC. Adsorptive desulfurization by activated alumina. J Hazard Mater, 2009, 170: 1133–1140

9   Hernández-Maldonado AJ, Yang RT. Desulfurization of commercial liquid fuels by selective adsorption *via* π-complexation with Cu(I)-Y zeolite. Ind Eng Chem Res, 2003, 42: 3103–3110

10 Gao J, Wang S, Jiang Z, *et al.* Deep desulfurization from fuel oil *via* selective oxidation using an amphiphilic peroxotungsten catalyst assembled in emulsion droplets. J Mol Catal A-Chem, 2006, 258: 261–266

11 Fang Y, Hu H. Mesoporous TS-1: nanocasting synthesis with CMK-3 as template and its performance in catalytic oxidation of aromatic thiophene. Catal Commun, 2007, 8: 817–820

12 Tam PS, Kittrell JR, Eldridge JW. Desulfurization of fuel oil by oxidation and extraction. 1. Enhancement of extraction oil yield. Ind Eng Chem Res, 1990, 29: 321–324

13 Bösmann A, Datsevich L, Jess A, *et al.* Deep desulfurization of diesel fuel by extraction with ionic liquids. Chem Commun, 2001, 26: 2494–2495

14 Gray KA, Pogrebinsky OS, Mrachko GT, *et al.* Molecular mechanisms of biocatalytic desulfurization of fossil fuels. Nat Biotech, 1996, 14: 1705–1709

15 Rashtchi M, Mohebali GH, Akbarnejad MM, *et al.* Analysis of biodesulfurization of model oil system by the bacterium, strain RIPI-22. Biochem Eng J, 2006, 29: 169–173

16 Fan J, Wang G, Sun Y, *et al.* Research on reactive adsorption desulfurization over $Ni/ZnO-SiO_2-Al_2O_3$ adsorbent in a fixed-fluidized bed reactor. Ind Eng Chem Res, 2010, 49: 8450–8460

17 Jun HK, Lee TJ, Kim JC. Role of iron oxide in the promotion of Zn-Ti-based desulfurization sorbents during regeneration at middle temperatures. Ind Eng Chem Res, 2002, 41: 4733–4738

18 Slimane RB, Abbasian J. Utilization of metal oxide-containing waste materials for hot coal gas desulfurization. Fuel Processing Tech, 2001, 70: 97–113

19 Tawara K, Nishimura T, Iwanami H, *et al.* New hydro-desulfurization catalyst for petroleum-fed fuel cell vehicles and cogenerations. Ind Eng Chem Res, 2001, 40: 2367–2370

20 Ullah R, Bai P, Wu P, *et al.* Superior performance of freeze-dried $Ni/ZnO-Al_2O_3$ adsorbent in the ultra-deep desulfurization of high sulfur model gasoline. Fuel Process Tech, 2016, 156: 505–514

21 Wen Y, Wang G, Wang Q, *et al.* Regeneration characteristics and kinetics of $Ni/ZnO-SiO_2-Al_2O_3$ adsorbent for reactive adsorption desulfurization. Ind Eng Chem Res, 2012, 51: 3939–3950

22 Meng X, Huang H, Shi L. Reactive mechanism and regeneration performance of $NiZnO/Al_2O_3$-diatomite adsorbent by reactive adsorption desulfurization. Ind Eng Chem Res, 2013, 52: 6092–6100

23 Efthimiadis EA, Sotirchos SV. Reactivity evolution during sulfidation of porous zinc oxide. Chem Eng Sci, 1993, 48: 829–843

24 Tawara K, Nishimura T, Iwanami H. Ultra-deep hydrodesulfurization of kerosene for fuel cell system (Part 2). Regeneration of sulfur-poisoned nickel catalyst in hydrogen and finding of auto-regenerative nickel catalyst.. Sekiyu Gakkaishi, 2000, 43: 114–120

25 Huang L, Wang G, Qin Z, *et al. In situ* XAS study on the mechanism of reactive adsorption desulfurization of oil product over Ni/ZnO. Appl Catal B-Environ, 2011, 106: 26–38

26 Wang L, Zhao L, Xu C, *et al.* Screening of active metals for reactive adsorption desulfurization adsorbent using density functional theory. Appl Surf Sci, 2017, 399: 440–450

27 Huang L, Wang G, Qin Z, *et al.* A sulfur K-edge XANES study on the transfer of sulfur species in the reactive adsorption desulfurization of diesel oil over Ni/ZnO. Catal Commun, 2010, 11: 592–596

28 Babich I. Science and technology of novel processes for deep desulfurization of oil refinery streams: a review. Fuel, 2003, 82: 607–631

29 Bezverkhyy I, Gadacz G, Bellat JP. Interaction of Ni/SiO$_2$ with thiophene. Mater Chem Phys, 2009, 114: 897–901

30 Bezverkhyy I, Ryzhikov A, Gadacz G, *et al.* Kinetics of thiophene reactive adsorption on Ni/SiO$_2$ and Ni/ZnO. Catal Today, 2008, 130: 199–205

31 Ryzhikov A, Bezverkhyy I, Bellat JP. Reactive adsorption of thiophene on Ni/ZnO: role of hydrogen pretreatment and nature of the rate determining step. Appl Catal B-Environ, 2008, 84: 766–772

32 Zhang J, Liu Y, Tian S, *et al.* Reactive adsorption of thiophene on Ni/ZnO adsorbent: effect of ZnO textural structure on the desulfurization activity. J Nat Gas Chem, 2010, 19: 327–332

33 Zhang Y, Kang Z, Yan X, *et al.* ZnO nanostructures in enzyme biosensors. Sci China Mater, 2015, 58: 60–76

34 Li LB, Wu WQ, Rao HS, *et al.* Hierarchical ZnO nanorod-on-nanosheet arrays electrodes for efficient CdSe quantum dot-sensitized solar cells. Sci China Mater, 2016, 59: 807–816

35 Gupta M, He J, Nguyen T, *et al.* Nanowire catalysts for ultra-deep hydro-desulfurization and aromatic hydrogenation. Appl Catal B-Environ, 2016, 180: 246–254

36 Liu Y, She N, Zhao J, *et al.* Fabrication of hierarchical porous ZnO and its performance in Ni/ZnO reactive-adsorption desulfurization. Pet Sci, 2013, 10: 589–595

37 Bai P, Wu P, Yan Z, *et al.* Self-assembly of clewlike ZnO superstructures in the presence of copolymer. J Phys Chem C, 2007, 111: 9729–9733

38 Ullah R, Zhang Z, Bai P, *et al.* One-pot cation-anion double hydrolysis derived Ni/ZnO-Al$_2$O$_3$ absorbent for reactive adsorption desulfurization. Ind Eng Chem Res, 2016, 55: 3751–3758

39 Emeis CA. Determination of integrated molar extinction coefficients for infrared absorption bands of pyridine adsorbed on solid acid catalysts. J Catal, 1993, 141: 347–354

40 Yang YX, Zhang YL, Lu W, et al. Ultra deep adsorptive desulfurization of solvent oils by Ni/ZnO adsorbent. Petrechem Tech, 2008, 3: 11

41 Ge H, Tang M, Wen XD, et al. Ni/ZnO nano sorbent for reactive adsorption desulfurization of refinery oil streams. In: Applying Nanotechnology to the Desulfurization Process in Petroleum Engineering. Pennsylvania: IGI Global, 2016, 216–239

42 Meng X, Weng HX, Shi L. Reactive adsorption of thiophene on ZnNi/diatomite-pseudo-boehmite adsorbents. China Pet Process Petrochem Tech, 2012, 14: 25–30

43 Petzold FG, Jasinski J, Clark EL, *et al.* Nickel supported on zinc oxide nanowires as advanced hydrodesulfurization catalysts. Catal Today, 2012, 198: 219–227

44 Yang HG, Zeng HC. Self-construction of hollow SnO$_2$ octahedra based on two-dimensional aggregation of nanocrystallites. Angew Chem, 2004, 116: 6056–6059

45 Li R, Wei Z, Zhao F, *et al.* Investigation of localized and delocalized excitons in ZnO/ZnS core-shell heterostructured nanowires. Nanophotonics, 2017, 6

46 Chung YT, Ba-Abbad MM, Mohammad AW, *et al.* Functionalization of zinc oxide (ZnO) nanoparticles and its effects on polysulfone-ZnO membranes. Desalination Water Treatment, 2016, 57: 7801–7811

47 Tang M, Zhou L, Du M, *et al.* A novel reactive adsorption desulfurization Ni/MnO adsorbent and its hydrodesulfurization ability compared with Ni/ZnO. Catal Commun, 2015, 61: 37–40

48 Ju F, Liu C, Meng C, *et al.* Reactive adsorption desulfurization of hydrotreated diesel over a Ni/ZnO-Al$_2$O$_3$–SiO$_2$ adsorbent. Energy Fuels, 2015, 29: 6057–6067

49 Bezverkhyy I, Safonova OV, Afanasiev P, *et al.* Reaction between thiophene and Ni nanoparticles supported on SiO$_2$ or ZnO: *in situ* synchrotron X-ray diffraction study. J Phys Chem C, 2009, 113: 17064–17069

50 Rouquerol F, Rouquerol J, Sing K. Adsorption by active carbons. In: Adsorption by Powders & Porous Solids Principles, Methodology and Applications. Oxford: Elsevier, 1999. 237–285

51 Groen JC, Peffer LAA, Pérez-Ramírez J. Pore size determination in modified micro- and mesoporous materials. Pitfalls and limitations in gas adsorption data analysis. Microporous Mesoporous Mater, 2003, 60: 1–17

52 Zhou H, Fan T, Zhang D. Hydrothermal synthesis of ZnO hollow spheres using spherobacterium as biotemplates. Microporous Mesoporous Mater, 2007, 100: 322–327

53 Sharma R, Alam F, Sharma AK, *et al.* ZnO anchored graphene hydrophobic nanocomposite-based bulk heterojunction solar cells showing enhanced short-circuit current. J Mater Chem C, 2014, 2: 8142–8151

54 Rema Devi BS, Raveendran R, Vaidyan AV. Synthesis and characterization of Mn^{2+}-doped ZnS nanoparticles. Pramana-J Phys, 2007, 68: 679–687

55 Trivedi MK, Tallapragada RM, Branton A, *et al.* Influence of biofield treatment on physical and structural characteristics of barium oxide and zinc sulfide. J Lasers Opt Photon, 2015, 2: 1000122

56 Meng W, Qi Z, Wei H, *et al.* Surface stoichiometry of zinc sulfide and its effect on the adsorption behaviors of xanthate. Chem Cent J, 2011, 5: 73

57 Wormsbecher RF, Kim G. Sulfur reduction in FCC gasoline. US Patent, 5525210, 1996-06-11

58 Yan Z, Fan J, Zuo Z, *et al.* NH$_3$ adsorption on the Lewis and Bronsted acid sites of MoO$_3$ (010) surface: a cluster DFT study. Appl Surf Sci, 2014, 288: 690–694

59 Meng X, Huang H, Weng H, *et al.* Ni/ZnO-based adsorbents supported on Al$_2$O$_3$, SiO$_2$, TiO$_2$, ZrO$_2$: a comparison for desulfurization of model gasoline by reactive adsorption. Bull Korean Chem Soc, 2012, 33: 3213–3217

60 Yang YL, Kou Y. Determination of the Lewis acidity of ionic liquids by means of an IR spectroscopic probe. Chem Commun, 2004, 10: 226–227

61 Kraleva E, Sokolov S, Schneider M, *et al.* Support effects on the properties of Co and Ni catalysts for the hydrogen production from bio-ethanol partial oxidation. Int J Hydrogen Energy, 2013, 38: 4380–4388

62 Denis A, Grzegorczyk W, Gac W, *et al.* Steam reforming of ethanol over Ni/support catalysts for generation of hydrogen for fuel cell applications. Catal Today, 2008, 137: 453–459

63 Chandra Srivastava V. An evaluation of desulfurization technologies for sulfur removal from liquid fuels. RSC Adv, 2012, 2: 759–783

64 Zhang J, Xu H, Jin X, *et al.* Characterizations and activities of the nano-sized Ni/Al$_2$O$_3$ and Ni/La-Al$_2$O$_3$ catalysts for NH$_3$ decomposition. Appl Catal A-General, 2005, 290: 87–96

Author contributions   Bai P conceived the idea and arranged the experiments; Liu B conducted the material synthesis and evaluated the adsorbents in RADS; Wu P, Ullah R, Xing W and Yan Z helped in the characterization of materials and data analysis. All authors contributed to the general discussion.

Conflict of interest   The authors declare that they have no conflict of interest.

Supplementary information   Supporting data are available in the online version of the paper.

Peng Bai received his PhD from China University of Petroleum (East China) in 2008. Then, he worked in National University of Singapore as a postdoctoral research fellow. Then he worked in the Institute of Chemical and Engineering Sciences, A*STAR, Singapore, as a scientist. He is currently an associate professor in China University of Petroleum (East China). His research interests focus on the development of porous materials for catalytic applications.

Bowen Liu is currently a master student at the College of Chemical Engineering, China University of Petroleum (East China). His research interest includes nanostructured adsorbents for reactive adsorption desulfurization.

Zifeng Yan received his PhD from Lanzhou Institute of Chemical Physics, Chinese Academy of Sciences in 1994. He is currently the Chair Professor of the State Key Laboratory of Heavy Oil Processing, PetroChina Key Laboratory of Catalysis, and a founding professor of chemical material and catalysis subjects in China University of Petroleum (East China). His research interests focus on the adsorption, catalysis and nanomaterial synthesis and application.

毛线球状ZnO超结构在反应吸附脱硫中的优异性能

白鹏[1*], 刘博文[1], 吴萍萍[1], Rooh Ullah[1], 邢伟[2], 阎子峰[1*]

摘要   本文利用共聚物控制均匀沉淀法自组装合成了一种毛线球状ZnO超结构. 通过将Ni浸渍于该氧化锌材料上制备了一系列Ni/ZnO吸附剂. 其中,样品Ni/ZnO-4h在反应吸附脱硫中表现出极高的硫容量(189.1 mg S g^{-1}),是相同条件下使用普通商业ZnO制备的Ni/ZnO-C样品的6倍. 毛线球状ZnO疏松开放的结构能够促进反应物/产物的扩散,并抑制体积膨胀对吸附剂结构的破坏. 较小的ZnO颗粒在提供较高的硫容量的同时还能促进活性组分Ni的分散,从而导致吸附剂具有较高的反应吸附脱硫性能.